ARTICLE

A Rational Study on the Geometric and Electronic Properties of Single-atom Catalysts for Enhanced Catalytic Performance

Received 00th January 20xx,
Accepted 00th January 20xx

DOI: 10.1039/x0xx00000x

Qi Xue[‡a], Yi Xie[‡b], Simson Wu[c], Tai-Sing Wu[d], Yun-Liang Soo[d], Sarah Day[e], Chiu C. Tang[e], Ho W. Man[a], Sha T. Yuen[b], Kwok-yin Wong[a], Ying Wang*[b], Benedict T.W. Lo*[a,f], Shik C.E. Tsang[c]

We investigate the geometric and electronic properties of single-atom catalysts (SACs) within metal-organic frameworks (MOFs) with respect to electrocatalytic CO_2 reduction as a model reaction. A series of mid-to-late 3d transition metals have been immobilised within the microporous cavity of UiO-66-NH_2. By employing Rietveld refinement of *new-generation* synchrotron diffraction, we not only identified the crystallographic and atomic parameters of the SACs that are stabilised with a robust M···N(MOF) bonding of *ca.* 2.0 Å, but also elucidated the end-on coordination geometry with CO_2. A volcano trend in the FEs of CO has been observed. In particular, the confinement effect within rigid MOF can greatly facilitate redox hopping between the Cu SACs, rendering high FEs of CH_4 and C_2H_4 at the current density of -100 mA cm^{-2}. Despite only demonstrated in selected SACs within UiO-66-NH_2, this study sheds light towards the rational engineering of molecular interactions(s) with SACs for the sustainable provision of fine chemicals.

Introduction

The design of modern catalysts is often inspired by the beautiful scaffolds and metal-containing cofactors in enzymes. The metal centres of many redox-active enzymes contain mid-to-late 3d transition metal ions due to the extensively variable oxidation states. The combination of electronic (redox of metal centres and binding strengths) and geometric properties (steric confinement and inert protein scaffold) leads to exceptional biological functionality and extremely high product selectivity in bio-catalysis.[1,2]

Significant research effort has been devoted to exploring the use of metal-organic frameworks (MOFs) and derivates in catalysis, such as for organic transformation reactions[3–5] and electrochemical conversion[6–9]. Besides catalysis, MOFs derived materials possess extensive applications in areas, such as cryogenic[10], electronics[11], battery[12], and flexible material[13,14].

Thanks to the wide tunability of MOFs, pristine MOFs can be modified by different approaches to incorporate single-atom catalysts (SACs).[15] Specific molecular functionalities (such as porphyrin, amine, sulphonate, thiol and various other defective sites) can be used to graft SACs [16–19] that are stabilised by the intrinsic acid-base interactions between Lewis acidic metal/cluster nodal centres and Lewis basic organic linkers, avoiding the metal sites from aggregation.[20,21] Highly homogeneous distribution of SACs can be therefore achieved within MOFs.[22,23] The incorporation of SACs onto crystalline MOFs can be put into two main categories: (1) Fabrication onto functional groups on the ligands, (2) Fabrication onto Lewis acid sites of the nodal centres (often defective).[24] Deposition onto ligands and nodal centres generally employ traditional acid-base coordination chemistry. Utilisation of the chemical functionalities of MOFs can be considered at the design stage. In addition, the functional groups and spatial properties play pivotal roles in controlling the stability (via tuning the bonding interactions) and reactivity (via tuning the geometric and electronic properties) of the supported SACs. In this present study, we specifically employed SACs supported on the ligand amino (-NH_2) moieties of UiO-66-NH_2 as model catalysts to investigate the electronic and geometric structures with respect to the catalytic properties of eCO_2RR.

The electronic structures of SACs, such as binding energies and reaction coordinates, have been suggested to be critical factors that govern catalytic properties.[25,26,27] For example, the conversion of CO_2 to CO was suggested to occur over Au, Ag and Pd metal electrocatalysts as they can bind the COOH* intermediate strongly, but bind CO* binding weakly.[28] Back *et al.* have predicted the eCO_2RR properties of a series of SACs on defective graphene based on theoretical calculations, where the electronic interactions between the d-orbital of the SACs

[a] *The Hong Kong Polytechnic University Shenzhen Research Institute, Shenzhen, China*
E-mail: benedict.tw.lo@polyu.edu.hk
[b] *Department of Chemistry, The Chinese University of Hong Kong, Hong Kong, China*
E-mail: ying.b.wang@cuhk.edu.hk
[c] *Department of Chemistry, University of Oxford, Oxford, OX1 3QR, UK*
[d] *Department of Physics, National Tsing Hua University, Hsinchu, Taiwan*
[e] *Diamond Light Source Ltd, Harwell Science and Innovation Campus, Didcot, Oxfordshire OX11 0DE, UK*
[f] *State Key Laboratory of Chemical Biology and Drug Discovery, Department of Applied Biology and Chemical Technology, The Hong Kong Polytechnic University, Hong Kong, China*
‡ *These authors contributed equally to this work as joint first authors.*
Electronic Supplementary Information (ESI) available: [details of any supplementary information available should be included here]. See DOI: 10.1039/x0xx00000x

and the p-orbital of graphene govern the density of state and hence the catalytic behaviours.[29] In addition, Li *et al.* reported a volcano trend in eCO_2RR toward the formation of CO over Mn-, Fe-, Co-, Ni- and Cu- SACs on defective graphene; the variation in selectivity has been ascribed to the difference in binding energies of SACs of CO_2^-* and H*. The geometric and electronic properties of the SACs, as well as the adsorbate structures of CO2, are therefore critical to extrapolate more accurate predictions for the design of more superior catalytic systems. However, it is challenging to experimentally determine this information due to the lack of appropriate characterisation techniques. Excitingly, our group has developed a reliable methodology that can elucidate the crystallographic locations and the adsorbate coordination information at atomistic resolution by combining synchrotron-based diffraction and absorption evidence.[30–32] The slight-but-significant alteration of the scattering factors in high-quality diffraction data has enabled us to determine the atomic parameters of the SACs and the tertiary structures with different substrate molecules.

It is noted that SACs supported on porous carbon and graphene materials show superior performance in catalysis and energy storage because of high conductivity and stability. However, due to the lack of long-range order, only limited techniques can offer reliable characterisation for SACs supported on carbon-based materials. Notably, electron microscopy and X-ray absorption spectroscopy are the two primary techniques used to reveal the single-atom nature of the metal sites in recent works.[33,34] An absence of M-M contribution from the EXAFS spectrum is usually indicative of SACs formation. Indeed, it is extremely challenging to probe the geometric property of the SACs with respect to the host materials using experimental techniques.

We, herein, employ crystalline UiO-66-NH_2 as the host to graft a series of mid-to-late *3d* transition metal ions (Fe, Co, Ni, Cu and Zn) by forming relatively stable Lewis acid-base adducts between the terminal amino -NH_2 group with extra-framework Lewis acidic metal ions. By Rietveld refinement of high-resolution diffraction data, the atomic parameters of the SACs in a three-dimensional manner can be reliably revealed. Over our model reaction of eCO_2RR, the two governing factors (i.e., geometric and electronic properties) related to the catalytic performance will be studied respectively. We will first elucidate the crystallographic locations of the SACs and determine their interactions with the host UiO-66-NH_2. The adsorption geometries and thermodynamic information of the activated metal···CO_2 guest complexes with respect to the metal SACs and MOF are also considered. By further studying the redox hopping property of the SACs by voltammetric extrapolation, their corresponding relationships with respect to the catalytic performance will be established.

Results and Discussion

Material Characterisation and Rietveld Refinement

Highly crystalline UiO-66-NH_2 powder sample has been prepared and characterised (see Figures S1-S5 in Supplementary Material). Based on the method reported by Lamberti et al., the extent of ligand defect in MOF can be calculated by calcination in air using thermogravimetric analysis.[35] As seen in Figure S1 the weight loss between 300 °C and 600 °C can be attributed to the combustion of organic linkers (2-aminoterephthalic acid, ATA) and the remaining weight can be ascribed to the presence of ZrO_2. Hence, the structural formula of the marginally defective sample is calculated to be $Zr_6O_4(OH)_4(ATA)_{5.8}$ (Zr:ATA = 1:0.96). The post-synthetic metalation conditions with Fe, Co, Ni, Cu and Zn have been well-controlled (see Methods/SI). We note the possibility of metal coordination to the defective sites of the Zr_6O_4 clusters, akin to the recent work reported by Yaghi *et al.*[24]; the marginally defective MOF can however only offer limited defects for metalation. No aggregated features on the particle surface or in the bulk structure can be observed from the microscopic measurements (Figures S3-S4). The elemental analysis has confirmed successful metalation (Table S1). As seen in the diffraction data, the space group remains at *Fm-3m* but the Bragg peak intensities change notably due to the incorporation of metal sites (Figure S5). We do not observe any appearance of new Bragg diffraction peaks, showing no trace of metal aggregation. Thanks to the significant difference in scattering factors between the MOF and the doped extra-framework metal species, the crystallographic locations can be determined precisely through the simulated annealing technique (performed using TOPAS v6.0). The Rietveld refinement results suggest that the extra-framework metal species interacts with the -NH_2 moiety of the MOF in a similar manner (Figure 1). The metal···N distances are found between 1.92 Å – 2.06 Å with the bond angles between 102° – 129°, indicative of the formation of Lewis acid-base adducts. The sp^3 character of the -$N(H_2)$ moiety makes the geometry of the complex nearly tetrahedral, *cf*. NH_4^+ (T_d). From the refined crystal structures, the atomically dispersed metal sites are comparable with each other in terms of bond lengths and angles. It is noted that the slight variation in the bond lengths can be ascribed to the difference in effective nuclear charge (Z_{eff}).

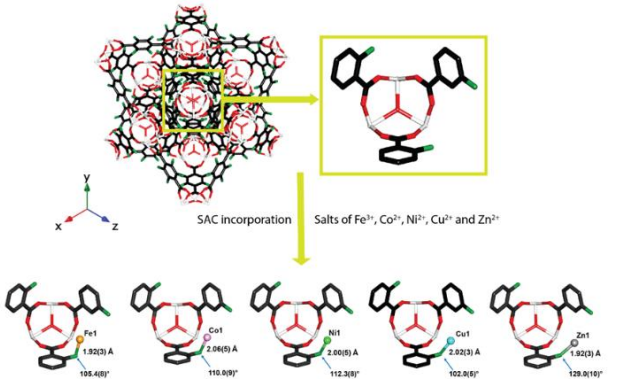

Figure 1. The crystal structures of 1Fe-, 1Co-, 1Ni-, 1Cu-, and 1Zn-UiO-66-NH_2 derived from Rietveld refinement of the high-resolution powder XRD data. The simulated annealing technique was applied using the TOPAS v6.0 academic software. The corresponding crystallographic and atomic parameters are presented in Tables S2-S3.

Using the Cu-modified UiO-66-NH_2 ('1Cu-UiO-66-NH_2') as an illustration (as it presents a more superior catalytic performance in eCO_2RR as later discussed), uniform distribution of Cu species is observed from the energy dispersive X-ray mapping analysis (Figure S4). Fourier-transform infrared (FTIR) spectroscopy has been applied to probe the Cu···N interaction between the Cu centre and the amino group. As seen in Figure 2a, a new peak at *ca.* 1050 cm^{-1} is observed, which can be attributed to the Cu-N stretching vibration.[36,37] The 1Cu-UiO-66-NH_2 sample exhibits high thermal and solvo-stabilities, as seen from the *in-situ* synchrotron diffraction measurements (Figures S6-S7) and elemental analysis (Table S1). The powder XRD pattern and the Cu content remains almost unchanged after being suspended in water at 80 °C for three hours (Table S1).

X-ray absorption spectroscopy can provide geometric information about the nature of the Cu site and its coordination environment. From our extended X-ray absorption fine structure spectroscopy (EXAFS) results (Figures 2b and S8, and Table S4), the Cu-O/N scattering path with an average coordination number (CN) of 4.2(2) and a bond length of 1.97(2) Å is obtained. It should be noted that Cu-O and Cu-N are hardly distinguishable by X-ray due to the small difference in the scattering factors. The absence of Cu-Cu contribution confirms that the Cu species are well dispersed. We have exploited the Cu bonding environment obtained to construct a more reliable initial rigid body Z-matrix for the subsequent Rietveld refinement. As a result, we have carefully considered a series of initial rigid body Z-matrices, consisting of (i) a Cu centre, (ii) one or two ligated ethylene diamine molecule(s) (with Cu-N at 1.95 Å), or (iii) one or two ligated water molecule(s) (with Cu-O at 1.95 Å) with different coordination environments, to model different coordination possibilities. During the Rietveld refinement process, both the bond angles and dihedral angles of Cu-O were gradually relaxed by simulated annealing for more accurate structural results. The oxidation state of Cu^{II} has been identified by X-ray absorption near edge structure spectroscopy (XANES, Figure 2c), where a broad pre-edge peak akin to Cu^{II} in CuO with a tetrahedral geometry can be observed.

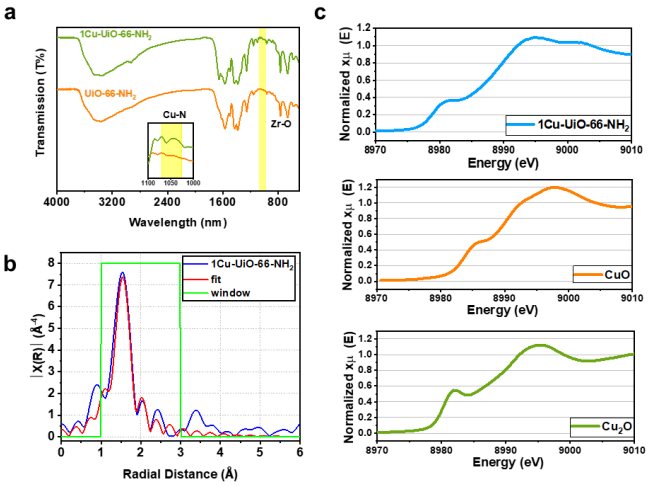

Figure 2. (a) FTIR spectra of UiO-66-NH_2 and 1Cu-UiO-66-NH_2. (b) k^3-weighted χ(R) function of the EXAFS of 1Cu-UiO-66-NH_2, indicating the absence of Cu-Cu contribution. (c) XANES, comparing 1Cu-UiO-66-NH_2 with CuO and Cu_2O.

The Rietveld refinement profile of the SXRD data of 1Cu-UiO-66-NH_2 and the corresponding crystal structure are presented in Figure 3. As seen in the Rietveld refined crystal structure in Figure 3b and 3c, the Cu1 site is located near the -NH_2 moiety of the linker, with an interatomic distance of 2.02(3) Å. The interatomic angle ∠C-N(MOF)···Cu is measured as 102.0(5)° and ∠ N(MOF)···Cu-O as 146.7(4)°. This interatomic information indicates that the Cu^{II} complex has a pseudo-tetrahedral geometry, with the ground state as e.[38] The Cu centre is bonded with the -NH_2 group *via* Lewis acid-base interaction. The Cu···N bond length of 2.02(3) Å suggests that the Lewis acid-base interaction is comparable with a typical Cu-N bond in metal complexes. In the Rietveld refinement process, the inclusion of the relatively larger 5-coordinated rigid body clashes with the MOF framework, suggesting that the unlikely presence of such a Cu-complex in the MOF cavity. This also verifies why the EXAFS analysis shows a lower total Cu CN of 4 than that of the Cu precursor of 6. The decrease in CN is commonly observed in typical Cu complexes due to steric effect; $[Cu(H_2O)_6]^{2+}$ (D_{4h}) becomes $[CuCl_4]^{2-}$ (nearly tetrahedral) upon Cl^- substitution.

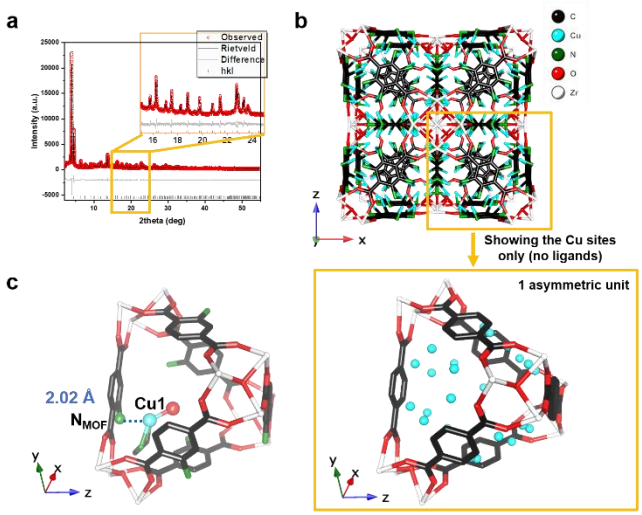

Figure 3. The Rietveld refinement of SXRD data of (a) 1Cu-UiO-66-NH_2 (at 15 keV; R_{wp} = 9.510%) and (b) the corresponding refined crystal structure. Zoom-in image of an asymmetric unit is shown, with all N atoms disregarded for clarity. The site occupancy factor of the Cu sites is 0.091(1). (c) The crystal structure of an asymmetric unit showing the interaction between MOF and the Cu complex. Atoms are presented in balls-and-sticks model. The mirror Cu sites are disregarded for clarity. The crystallographic and atomic parameters are summarised in Table S3

Electronic Properties by Voltammetric Measurements

The electronic properties certainly play an active role in the catalytic properties. We note that our post-synthetic modification could only marginally affect the conductivities of the catalysts. Promotion effects in various MOF-driven electrochemical applications have been ascribed to redox hopping.[39,40] Redox hopping is a self-exchange charge transfer process between metal redox centres. It refers to the intrinsically redox-active metal centres/nodes or ligands, or the extra-framework energetically accessible redox sites.[41] Redox hopping can facilitate charge propagation from the electrode to the catalytic centres, which enhances the supply of necessary electrons for catalytic processes.[40]

We evaluate the redox hopping property of the samples using cyclic voltammetry (CV) at different scan rates (Figure S9), *cf.* the Cottrell equation[40]:

$$\mathrm{I(t)} = \mathrm{nFAC}D_{hopping}^{1/2}\pi^{-1/2}t^{-1/2}$$

The redox hopping coefficients, $D_{hopping}$, can be extrapolated by plotting I(t) (current density) *vs* $t^{-1/2}$ (scanning time), see Table 1 and Figure S10. $D_{hopping}$ of UiO-66-NH_2 was determined as 0.626 $m^2 s^{-1}$. Upon the addition of metal sites, for 1Fe-, 1Co-, 1Ni-, 1Zn-UiO-66-NH_2, $D_{hopping}$ increase slightly ranging between 0.776 m^2 s^{-1} and 0.925 m^2 s^{-1}. In contrast, $D_{hopping}$ of 1Cu-UiO-66-NH_2 increases by 168% to 1.683 m^2 s^{-1}, showing a significant improvement in redox hopping. The redox hopping observed in the pristine UiO-66-NH_2 sample can be ascribed to the electronic movement between the Zr_6O_4 nodal centre and the ATA acid linker. We can therefore attribute the promotional effect in redox hopping to the extra-framework energetically SACs, with Cu being the most active modifier.[41] The metal···N_{MOF} contribution on the electrocatalytic performance is evident.

Upon an applied potential, electrons move rapidly between nearby SACs in the form of $M^{(n+1)+}/M^{n+}$ redox reactions. As presented in Table S1, there are more than four statistical units of SACs per unit cell of UiO-66-NH_2 by taking the multiplicity factor (×48) of the *Fm-3m* space group into account. As a unit cell of UiO-66-NH_2 is *ca*. 20.8 Å in each dimension, the SACs are highly atomically dispersed, but they locate within a reasonable distance that can allow electron movement. The greatly enhanced redox hopping between the SACs can hence facilitate the reduction of adsorbed CO_2 to form $CO_2^{\cdot-}$ intermediate, followed by subsequent reactions to form CO and CH_4 products.

Table 1. The $D_{hopping}$ coefficients, derived from the Cottrell equation by plotting I(t) *vs* $t^{-1/2}$, of UiO-66-NH_2, 1Fe-, 1Co-, 1Ni-, 1Cu-, and 1Zn-UiO-66-NH_2.

Sample	$D_{hopping}$ ($m^2 s^{-1}$)
UiO-66-NH_2	0.626
1Fe-UiO-66-NH_2	0.834
1Co-UiO-66-NH_2	0.776
1Ni-UiO-66-NH_2	0.804
1Cu-UiO-66-NH_2	1.683
1Zn-UiO-66-NH_2	0.925

CO_2 Coordination with the SACs

Alongside the promoted redox hopping property, it is known that the Lewis acidic SACs can activate CO_2 *via* terminal O adsorption.[42] As demonstrated in our previous works, we have reliably determined the adsorbate structures of various small organic molecules in crystalline microporous materials.[30,43] Herein, we thus employed high-resolution high-energy X-ray (Mo X-ray anode; λ = 0.7107 Å) for Rietveld refinement to elucidate the adsorbate structures of CO_2 with respect to UiO-66-NH_2 and 1Cu-UiO-66-NH_2. The samples were pre-adsorbed with CO_2 carefully and loaded into a 0.5-mm borosilicate capillary to minimise X-ray absorption. Over the 2θ range of 2-30°, spinning samples have been collected at 1 mdeg step for 3 hours to ensure diffraction data with high signal-to-noise ratio and good counting statistics.

The Rietveld refinement profiles of CO_2 pre-adsorbed on UiO-66-NH_2 and 1Cu-UiO-66-NH_2 are presented in Figure 4. From the corresponding refined crystal structures (Figure 4c), the CO_2 adsorbate interacts with the framework amino -NH_2 moiety *via* a side-on mode in pristine UiO-66-NH_2, *cf.* N_{MOF}…C_{CO2} = 2.66(5) Å, N_{MOF}-(H)…O_{1CO2} = 2.70(5) Å and N_{MOF}- (H)…O_{2CO2} = 3.14(7) Å. For 1Cu-UiO-66-NH_2 (Figure 4d), the CO_2 adsorbate interacts with the Cu-O(H) *via* an end-on mode, where the entire CO_2 molecule aligns almost linearly with the Cu-O(H) bond; *cf.* O_{Cu}-(H)…O_{1CO2} = 3.39(6) Å, ∠$O_{Cu\text{-}complex}$-$O1_{CO2}$-C_{CO2} = 179(1)° and ∠Cu1-$O_{Cu\text{-}complex}$-$O1_{CO2}$ = 130(1)°. The interatomic distance falls in the H-bonding regime (typically between 1.5-2.5 Å[44]) by taking the O-H bond length of *ca*. 1.0 Å into consideration. It is believed that the steric confinement effect of the MOF

framework is pivotal in stabilising and crystallising the adsorbate CO_2 molecules. These findings are consistent with the previous report by Yang *et al.* that presented the side-on CO_2 adsorption geometry with an amine-functionalised MOF and the end-on CO_2 mode with a hydroxyl-functionalised MOF.[45]

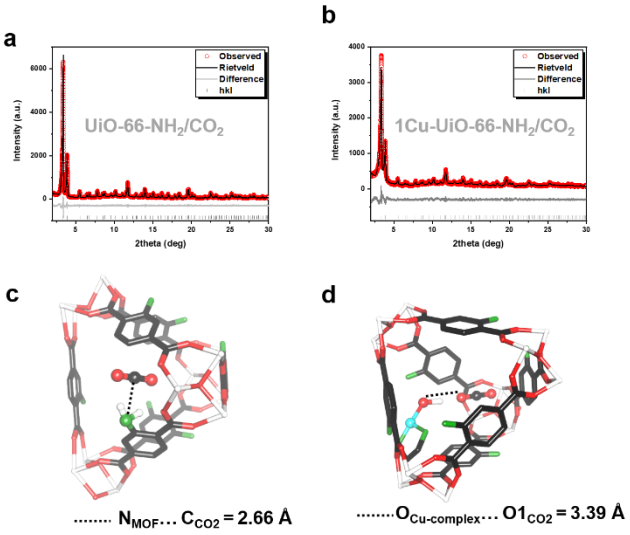

Figure 4. The Rietveld refinement of high-resolution powder XRD data (Mo X-ray, λ = 0.7107 Å) of (a) 1Cu-UiO-66-NH_2 and (b) 1Cu-UiO-66-NH_2 pre-adsorbed with CO_2. The corresponding derived crystal structures are presented in (c) and (d). The mirror N, Cu atoms and CO_2 molecules disregarded for clarity. Atoms are presented in balls-and-sticks model.

We further employed *in-situ* powder XRD measurements (in capillary geometry) to study the temperature-programmed desorption behaviour of CO_2 from the MOF frameworks (Figures 5 and S11). The effect of additional CO_2 can be seen directly from the dynamic change in the Bragg peak intensities. Notably, the drastic change in the intensity of (111) begins at 140 °C without pre-adsorbed CO_2, but it begins at 125 °C with CO_2, which agrees consistent with the thermogravimetric analysis result (Figure S12). The rise in Bragg peak intensities in the early 2θ range is typically attributed to the removal of species from the micropores.[46] Apparently, once the weakly adsorbed species are removed, the behaviours at the high-temperature regime (Figures 5a and 5b) are comparable to each other. The thermochemical study suggests that the adsorption of CO_2 is relatively strong on 1Cu-UiO-66-NH_2, which should be ascribed to the direct coordination to the Cu-OH, as shown in Figure 4. Similar trends in the change in the refined lattice parameters are observed (Figure 5c), where *a* first increases by *ca*. 0.1% with elevated temperature due to thermal expansion, followed by steady contraction due to the removal of adsorbed species. However, at the low-temperature range (25 – 100 °C), the lattice parameter values are lower with the inclusion of CO_2. It suggests that the H-bonded CO_2 in 1Cu-UiO-66-NH_2 plays a major role in limiting the expansion at the low-temperature range, due to the additional electrostatic interactions with the MOF structure.

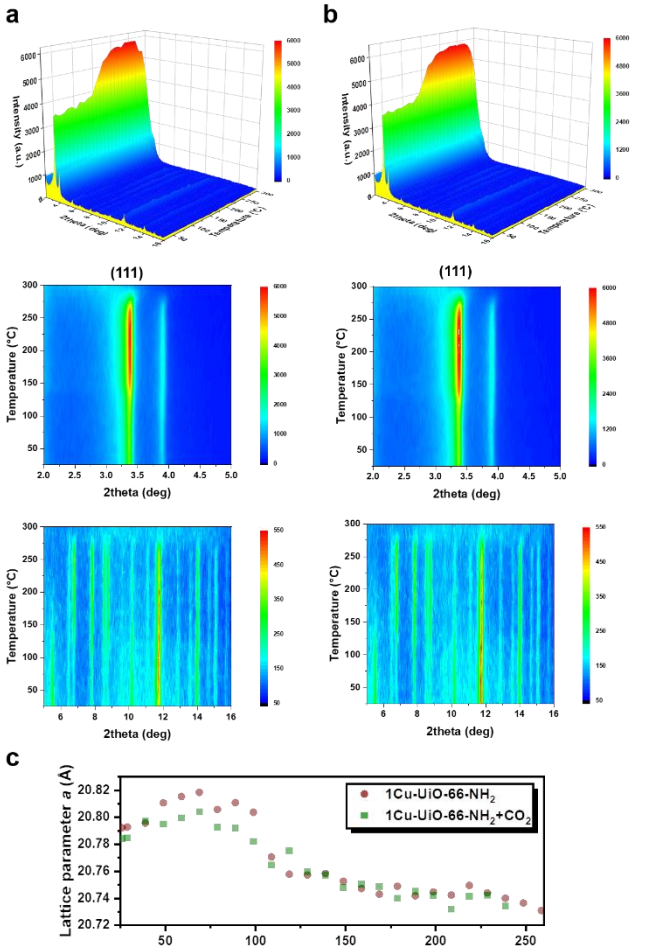

Figure 5. The *in-situ* XRD-temperature-programmed desorption measurements and the corresponding contour plots of (a) 1-Cu-UiO-66-NH_2 and (b) 1-Cu-UiO-66-NH_2 with pre-adsorbed CO_2. Apparent differences in the shape of the desorption profiles can be observed. The dynamic change of the refined lattice parameters *a* is shown in (c). The detailed crystallographic parameters are summarised in Tables S5-S6.

The Performance of Model eCO_2RR

The incorporation of the single sites can form cationic metal species and consequently making the sites Lewis acidic. Supported cationic metal sites can interact with the lone pair electrons on the terminal O moieties of incoming CO_2 molecules, which can not only activate the CO_2 more subsequent reactions but also stabilise the reaction intermediates (e.g. $CO_2^{\cdot-}$)[42]. To fully correlate the geometric and electronic properties with catalysis, we conducted model eCO_2RR experiments over the as-synthesised SACs within UiO-66-NH_2. Only H_2 and a trace amount of CO was found over UiO-66-NH_2 and the pristine carbon paper electrode (Table S7). The Faradaic efficiencies (FEs) of gaseous products changes noticeably over the metal-doped UiO-66-NH_2. The FE of CO increases significantly from <1% to *ca*. 10% for 1Co-, 1Ni- and 1Zn-UiO-66-NH_2 at 100 s at a current density of -100 mA cm^{-2} with an applied potential of *ca*. -1.0 V *vs* the reversible hydrogen electrode (RHE) (Figure 6a). The FE

of CO over 1Cu-UiO-66-NH_2 is less than 3%. A small proportion (<4%) of CH_4 is also produced over 1Co- and 1Zn-UiO-66-NH_2.

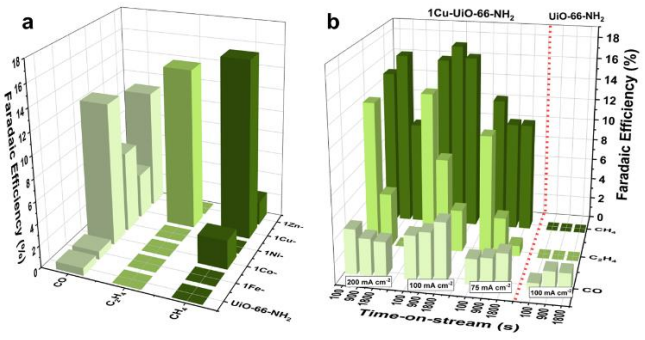

Figure 6. (a) The catalytic performance of eCO_2RR over UiO-66-NH_2 and incorporated with different SACs loaded on carbon paper as the electrode at -100 mA cm^{-2}. (b) The catalytic performance of eCO_2RR over UiO-66-NH_2 and 1Cu-UiO-66-NH_2 showing the time-resolved FEs at different current densities.

For 1Cu-UiO-66-NH_2, the product distribution is notably different from those over 1Fe-, 1Co-, 1Ni-, and 1Zn-UiO-66-NH_2. We identified multielectron transfer products (>4e^-; CH_4 and C_2H_4) with FEs of 16.1% and 14.6%, respectively at 100 s at a current density of -100 mA cm^{-2} with an applied potential of -0.96 V *vs* RHE. Over longer time-on-stream (Figure 6b), the FE of CH_4 remains stable for about an hour (Figure S13), whereas the FE of C_2H_4 decreases noticeably. Although the competing hydrogen evolution reaction is unavoidable, we have greatly reduced the FE of H_2 on 1Cu-UiO-66-NH_2 from 75.1% (on carbon paper) and 48.5% (on UiO-66-NH_2) to below 30%. The FEs of the liquid products with minor contribution are summarised in Table S8. The electrochemical catalytic activities were evaluated at different current densities from -75 mA cm^{-2} to -200 mA cm^{-2}. These catalytic findings are consistent with previous reports that SACs can promote eCO_2RR *via* enhanced CO_2 coordination and electronic modification.[47] Alongside the inverted 'volcano' trend of the FE of CO, the high FEs of CH_4 and C_2H_4 over 1Cu-UiO-66-NH_2 indicates the optimum binding of CO* with the Cu sites, consistent with the computational findings by Yang *et al.*[48] Our catalytic results are consistent with the recent report by Li *et al.*[49], where a similar volcano trend is also observed for the eCO_2RR toward CO product over a series of 3d transition metal SACs. In both cases, the Cu SACs give the lowest FE of CO due to the optimum binding of CO*, which may allow subsequent reduction reactions to form other multielectron products.

It should be noted that the electrocatalysts are relatively stable under the electrochemical conditions, as seen in the time-resolved product distribution (Figure S13). Also, we have not observed any evidence of SAC aggregation after 1 hour of time-on-stream, and the crystallinity of the sample only decreases slightly as seen from powder XRD and electron diffraction evidence (Figures S14 and S15).

Conclusion

Significant research effort has been devoted to the design and utilisation of SACs in various catalytic applications. In this article, we studied both the geometric and electronic properties of a series mid-to-late *3d* transition metal SACs within UiO-66-NH_2. Based on the crystal structures derived from Rietveld refinement of high-resolution powder XRD measurements, these SACs all form similar Lewis acid-base adduct complexes with the framework -NH_2 groups. Akin to many examples in bio-catalysis, the steric confinement of the scaffold hinders the change in symmetry of the active metal centres. A notable example is the Cu^{II}/Cu^{I} redox couple that is facilitated by the rigid coordination environment of the Cu centres in plastocyanin protein. It is therefore anticipated that the $M^{(n+1)+}/M^{n+}$ redox couple can promote eCO_2RR due to the rigid framework scaffold of UiO-66-NH_2 (with a pore size of *ca*. 6 Å). This effect is particularly profound in the case of Cu^{II}/Cu^{I}, which leads to a more superior catalytic property of 1Cu-UiO-66-NH_2 that gives high FEs of CH_4 and C_2H_4. The eCO_2RR process includes adsorption, electron transfer, and desorption. In this work, we extensively discussed the relationship of the geometric structures and electronic properties of the supported SACs with respect to eCO_2RR. We correlated 'geometric structures' with the atomic parameters of the SACs and the adsorbate structures in terms of interatomic distances and angles with respect to the support. In particular, akin to enzyme systems, the tertiary structure with substrate molecule(s) will determine the spatial conformation that affect the catalytic properties. Meanwhile, we primarily correlated 'electronic properties' with the redox hopping behaviour of the metal sites which has been studied through cyclic voltammetry. Clearly, not only the geometric structures, but the electronic properties are also critical in governing the catalytic properties of eCO_2RR. We warrant that the work will lay a solid foundation for the future design of SACs and related materials for the sustainable provision of fine chemicals.

Conflicts of interest

There are no conflicts to declare.

Acknowledgements

This work was supported by the National Natural Science Foundation of China (21902139) and the Hong Kong Research Grants Council (25300918 and 15300819) for financial support (TWBL). YW thank the Science and Technology Planning Project of Guangdong Province (2019A050510018) for financial support. We thank SPring-8 (2018B1081), Diamond (NT23230-1) TPS (BL44A) for the provision of beamtime, and UMF, UCEA and ULS of HKPU for the support in material characterisation.

References

1 B. E. Kim, T. Nevitt and D. J. Thiele, *Nature Chemical Biology*, 2008, **4**, 176–185.

2 G. Kichin, C. Weiss, C. Wagner, F. S. Tautz and R. Temirov, *Journal of the American Chemical Society*, 2011, **133**, 16847–16851.

3 I. Luz, F. X. L. i Xamena and A. Corma, *Journal of Catalysis*, 2010, **276**, 134–140.

4 L. Sun, Q. Shao, Y. Zhang, H. Jiang, S. Ge, S. Lou, J. Lin, J. Zhang, S. Wu, M. Dong and Z. Guo, *Journal of Colloid and Interface Science*, 2020, **565**, 142–155.

5 Z. Sun, X. Wu, K. Qu, Z. Huang, S. Liu, M. Dong and Z. Guo, *Chemosphere*, 2020, **259**, 127389.

6 H. Zhang, J. Li, Q. Tan, L. Lu, Z. Wang and G. Wu, *Chemistry–A European Journal*, 2018, **24**, 18137–18157.

7 Z. Cai, P. Wang, J. Yang and X. Wang, *ES Energy & Environment*, , DOI:10.30919/esee8c320.

8 P. Yang, H. Zhao, Y. Yang, P. Zhao, X. Zhao and L. Yang, *ES Materials & Manufacturing*, , DOI:10.30919/esmm5f618.

9 X. Zhang, K. S. Ziemer and B. L. Weeks, *Advanced Composites and Hybrid Materials*, 2019, **2**, 492–500.

10 Y. He, Q. Chen, S. Yang, C. Lu, M. Feng, Y. Jiang, G. Cao, J. Zhang and C. Liu, *Composites Part A: Applied Science and Manufacturing*, 2018, **108**, 12–22.

11 Y. Lv, L. Zhu, H. Xu, L. Yang, Z. Liu, D. Cheng, X. Cao, J. Yun and D. Cao, *Engineered Science*, , DOI:10.30919/es8d768.

12 Y. Wang, Y. Liu, C. Wang, H. Liu, J. Zhang, J. Lin, J. Fan, T. Ding, J. E. Ryu and Z. Guo, *Engineered Science*, , DOI:10.30919/es8d903.

13 P. Feng, L. Ma, G. Wu, X. Li, M. Zhao, L. Shi, M. Wang, X. Wang and G. Song, *Composites Science and Technology*, 2020, **200**, 108336.

14 M. Ul-Islam, J. Ali, W. Khan, A. Haider, N. Shah, M. W. Ahmad, M. W. Ullah and G. Yang, *Engineered Science*, , DOI:10.30919/es8d504.

15 P. Ling, J. Lei, L. Jia and H. Ju, *Chemical Communications*, 2016, **52**, 1226–1229.

16 M. Y. Masoomi, A. Morsali, A. Dhakshinamoorthy and H. Garcia, *Angewandte Chemie - International Edition*, 2019, **58**, 15188–15205.

17 L. Wang, X. Qu, Y. Zhao, Y. Weng, G. I. N. Waterhouse, H. Yan, S. Guan and S. Zhou, *ACS applied materials & interfaces*, 2019, **11**, 35228–35237.

18 F. Xiao, G.-L. Xu, C.-J. Sun, M. Xu, W. Wen, Q. Wang, M. Gu, S. Zhu, Y. Li and Z. Wei, *Nano Energy*, 2019, **61**, 60–68.

19 B. Gui, K.-K. Yee, Y.-L. Wong, S.-M. Yiu, M. Zeller, C. Wang and Z. Xu, *Chemical Communications*, 2015, **51**, 6917–6920.

20 S. Mukherjee, B. Manna, A. V. Desai, Y. Yin, R. Krishna, R. Babarao and S. K. Ghosh, *Chemical Communications*, 2016, **52**, 8215–8218.

21 S. ichiro Noro, S. Kitagawa, T. Akutagawa and T. Nakamura, *Progress in Polymer Science (Oxford)*, 2009, **34**, 240–279.

22 Z. Liang, C. Qu, D. Xia, R. Zou and Q. Xu, *Angewandte Chemie - International Edition*, 2018, **57**, 9604–9633.

23 M. Ranocchiari and J. A. Van Bokhoven, *Physical Chemistry Chemical Physics*, 2011, **13**, 6388–6396.

24 A. M. Abdel-Mageed, B. Rungtaweevoranit, M. Parlinska-Wojtan, X. Pei, O. M. Yaghi and R. Jürgen Behm, *Journal of the American Chemical Society*, 2019, **141**, 5201–5210.

25 F. Pan, X. Xiang and Y. Li, *Engineered Science*, , DOI:10.30919/es.1804232.

26 C. Zhang, Y. Xie, H. Deng, C. Zhang, J. Su and J. Lin, *Engineered Science*, , DOI:10.30919/es8d516.

27 L. Liu, P. Bernazzani, W. Chu, S.-Z. Luo, B. Wang and Z. Guo, *Engineered Science*, , DOI:10.30919/es8d637.

28 W. Zhang, Y. Hu, L. Ma, G. Zhu, Y. Wang, X. Xue, R. Chen, S. Yang and Z. Jin, *Advanced Science*, , DOI:10.1002/advs.201700275.

29 S. Back, J. Lim, N.-Y. Kim, Y.-H. Kim and Y. Jung, *Chemical science*, 2017, **8**, 1090–1096.

30 B. T. W. Lo, L. Ye and S. C. E. Tsang, *Chem*, 2018, **4**, 1–31.

31 B. T. W. Lo, L. Ye, J. Qu, J. Sun, J. Zheng, D. Kong, C. A. Murray, C. C. Tang and S. C. E. Tsang, *Angewandte Chemie - International Edition*, 2016, **55**, 5981–5984.

32 T. Chen, B. Huang, S. Day, C. C. Tang, S. C. E. Tsang, K. yin Wong and T. W. B. Lo, *Angewandte Chemie - International Edition*, 2020, **59**, 1093–1097.

33 X. Wang, Z. Chen, X. Zhao, T. Yao, W. Chen, R. You, C. Zhao, G. Wu, J. Wang, W. Huang, J. Yang, X. Hong, S. Wei, Y. Wu and Y. Li, *Angewandte Chemie*, 2018, **130**, 1962–1966.

34 Y. Xiong, J. Dong, Z. Q. Huang, P. Xin, W. Chen, Y. Wang, Z. Li, Z. Jin, W. Xing, Z. Zhuang, J. Ye, X. Wei, R. Cao, L. Gu, S. Sun, L. Zhuang, X. Chen, H. Yang, C. Chen, Q. Peng, C. R. Chang, D. Wang and Y. Li, *Nature Nanotechnology*, , DOI:10.1038/s41565-020-0665-x.

35 L. Valenzano, B. Civalleri, S. Chavan, S. Bordiga, M. H. Nilsen, S. Jakobsen, K. P. Lillerud and C. Lamberti, *Chemistry of Materials*, 2011, **23**, 1700–1718.

36 J. Du, Y. Zhao, J. Chen, P. Zhang, L. Gao, M. Wang, C. Cao, W. Wen and C. Zhu, *RSC Advances*, 2017, **7**, 33929–33936.

37 Y. Ma, Y. Cen, M. Sohail, G. Xu, F. Wei, M. Shi, X. Xu, Y. Song, Y. Ma and Q. Hu, *ACS Applied Materials and Interfaces*, 2017, **9**, 33011–33019.

38 E. Garribba and G. Micera, *Journal of chemical education*, 2006, **83**, 1229.

39 I. Liberman, R. Shimoni, R. Ifraemov, I. Rozenberg, C. Singh and I. Hod, *Journal of the American Chemical Society*, 2020, **142**, 1933–1940.

40 S. Lin, P. M. Usov and A. J. Morris, *Chemical Communications*, 2018, **54**, 6965–6974.

41 L. Sun, M. G. Campbell and M. Dincă, *Angewandte Chemie International Edition*, 2016, **55**, 3566–3579.

42 X. Zu, X. Li, W. Liu, Y. Sun, J. Xu, T. Yao, W. Yan, S. Gao, C. Wang, S. Wei and Y. Xie, *Advanced Materials*, 2019, **31**, 1808135.

43 P. Zhao, L. Ye, Z. Sun, B. T. W. Lo, H. Woodcock, C. Huang, C. Tang, A. I. Kirkland, D. Mei and S. C. Edman Tsang, *Journal of the American Chemical Society*, 2018, **140**, 6661–6667.

44 P. T. A. Galek, L. Fábián and F. H. Allen, *CrystEngComm*, 2010, **12**, 2091–2099.

45 S. Yang, J. Sun, A. J. Ramirez-Cuesta, S. K. Callear, W. I. F. David, D. P. Anderson, R. Newby, A. J. Blake, J. E. Parker, C. C. Tang and M. Schröder, *Nature Chemistry*, 2012, **4**, 887–894.

46 A. W. Chester and E. G. Derouane, *Zeolite characterization and catalysis: A tutorial*, Springer, 2010.

47 J. Li, P. Prslja, T. Shinagawa, A. J. Martín Fernández, F. Krumeich, K. Artyushkova, P. Atanassov, A. Zitolo, Y. Zhou and R. García-Muelas, *ACS Catalysis*, 2019, **9**, 10426–10439.

48 H. Yang, Y. Wu, G. Li, Q. Lin, Q. Hu, Q. Zhang, J. Liu and C. He, *Journal of the American Chemical Society*, 2019, **141**, 12717–12723.

49 W. Zhang, Y. Hu, L. Ma, G. Zhu, Y. Wang, X. Xue, R. Chen, S. Yang and Z. Jin, *Advanced Science*, 2018, **5**, 1700275.

